AFRL-RV-PS-
TR-2017-0090

DESIGN AND FABRICATION OF HIGH-PERFORMANCE LWIR PHOTODETECTORS BASED ON TYPE-II SUPERLATTICES

Manijeh Razeghi

Northwestern University
2220 Campus Dr., Rm. 4051
Evanston, IL 60208-0893

11 Aug 2017

Final Report

APPROVED FOR PUBLIC RELEASE; DISTRIBUTION IS UNLIMITED.

AIR FORCE RESEARCH LABORATORY
Space Vehicles Directorate
3550 Aberdeen Ave SE
AIR FORCE MATERIEL COMMAND
KIRTLAND AIR FORCE BASE, NM 87117-5776

DTIC COPY
NOTICE AND SIGNATURE PAGE

Using Government drawings, specifications, or other data included in this document for any purpose other than Government procurement does not in any way obligate the U.S. Government. The fact that the Government formulated or supplied the drawings, specifications, or other data does not license the holder or any other person or corporation; or convey any rights or permission to manufacture, use, or sell any patented invention that may relate to them.

This report is the result of contracted fundamental research which is exempt from public affairs security and policy review in accordance with AFI 61-201, paragraph 2.3.5.1. This report is available to the general public, including foreign nationals. Copies may be obtained from the Defense Technical Information Center (DTIC) (http://www.dtic.mil).

AFRL-RV-PS-TR-2017-0090 HAS BEEN REVIEWED AND IS APPROVED FOR PUBLICATION IN ACCORDANCE WITH ASSIGNED DISTRIBUTION STATEMENT.

//SIGNED//
DAVID CARDIMONA
Program Manager

//SIGNED//
DAVID CARDIMONA
Technical Advisor, Space Based Advanced Sensing and Protection

//SIGNED//
JOHN BEAUCHEMIN
Chief Engineer, Spacecraft Technology Division
Space Vehicles Directorate

This report is published in the interest of scientific and technical information exchange, and its publication does not constitute the Government's approval or disapproval of its ideas or findings.

Approved for public release; distribution is unlimited.

REPORT DOCUMENTATION PAGE

Form Approved
OMB No. 0704-0188

Public reporting burden for this collection of information is estimated to average 1 hour per response, including the time for reviewing instructions, searching existing data sources, gathering and maintaining the data needed, and completing and reviewing this collection of information. Send comments regarding this burden estimate or any other aspect of this collection of information, including suggestions for reducing this burden to Department of Defense, Washington Headquarters Services, Directorate for Information Operations and Reports (0704-0188), 1215 Jefferson Davis Highway, Suite 1204, Arlington, VA 22202-4302. Respondents should be aware that notwithstanding any other provision of law, no person shall be subject to any penalty for failing to comply with a collection of information if it does not display a currently valid OMB control number. **PLEASE DO NOT RETURN YOUR FORM TO THE ABOVE ADDRESS.**

1. REPORT DATE *(DD-MM-YY)*	**2. REPORT TYPE**	**3. DATES COVERED** *(From - To)*
11-08-2017	Final Report	4 Mar 2016 – 2 Jun 2017

4. TITLE AND SUBTITLE
Design and Fabrication of High-Performance LWIR Photodetectors Based on Type-II Superlattices

5a. CONTRACT NUMBER
FA9453-16-1-0036

5b. GRANT NUMBER

5c. PROGRAM ELEMENT NUMBER
62601F

6. AUTHOR(S)
Manijeh Razeghi

5d. PROJECT NUMBER
4846

5e. TASK NUMBER
PPM00018191

5f. WORK UNIT NUMBER
EF127460

7. PERFORMING ORGANIZATION NAME(S) AND ADDRESS(ES)
Northwestern University
2220 Campus Dr., RM 4051
Evanston, IL 60208-0893

8. PERFORMING ORGANIZATION REPORT NUMBER

9. SPONSORING / MONITORING AGENCY NAME(S) AND ADDRESS(ES)
Air Force Research Laboratory
Space Vehicles Directorate
3550 Aberdeen Ave., SE
Kirtland AFB, NM 87117-5776

10. SPONSOR/MONITOR'S ACRONYM(S)
AFRL/RVSW

11. SPONSOR/MONITOR'S REPORT NUMBER(S)
AFRL-RV-PS-TR-2017-0090

12. DISTRIBUTION / AVAILABILITY STATEMENT

Approved for public release; distribution is unlimited.

13. SUPPLEMENTARY NOTES

14. ABSTRACT

Antimonide-based Type-II superlattices represent the most promising material system capable of delivering more producible, large-format, reduced pixel pitch, long-wavelength infrared (LWIR) focal plane arrays (FPAs) for persistent surveillance applications. Improvement in material quality and processing technique, as well as evolutionary modifications in device architecture have demonstrated the advantages of the material system over alternatives, and proven it as a viable candidate for the next generation infrared imaging.

15. SUBJECT TERMS

Focal plane array, improved minority carrier lifetime, type II superlattice and infrared

16. SECURITY CLASSIFICATION OF:			**17. LIMITATION OF ABSTRACT**	**18. NUMBER OF PAGES**	**19a. NAME OF RESPONSIBLE PERSON**
a. REPORT	**b. ABSTRACT**	**c. THIS PAGE**			David Cardimona
Unclassified	Unclassified	Unclassified	Unlimited	22	**19b. TELEPHONE NUMBER** *(include area code)*

(This page intentionally left blank)

Approved for public release; distribution is unlimited.

Table of Contents

Approved for public release; distribution is unlimited.

List of Figures

Approved for public release; distribution is unlimited.

ACKNOWLEDGMENTS

This material is based on research sponsored by Air Force Research Laboratory under agreement number FA9453-16-1-0036. The U.S. Government is authorized to reproduce and distribute reprints for Governmental purposes notwithstanding any copyright notation thereon.

DISCLAIMER

The views and conclusions contained herein are those of the authors and should not be interpreted as necessarily representing the official policies or endorsements, either expressed or implied, of the Air Force Research Laboratory or the U.S. Government.

Approved for public release; distribution is unlimited.

(This page intentionally left blank)

Approved for public release; distribution is unlimited.

1. SUMMARY

Antimonide-based Type-II superlattices represent the most promising material system capable of delivering more producible, large-format, reduced pixel pitch, long-wavelength infrared (LWIR) focal plane arrays (FPAs) for persistent surveillance applications. Improvement in material quality and processing technique, as well as evolutionary modifications in device architecture have demonstrated the advantages of the material system over alternatives, and proven it as a viable candidate for the next generation infrared imaging. Yet, the performance of this material system has not reached its limits.

2. INTRODUCTION

In this project, we propose to study both InAs/GaSb and strain-balanced $InAs_{1-x}Sb_x$/InAs Type-II superlattices for LWIR detection and imaging. After this study, it is expected to achieve a superlattice design with longer minority carrier lifetime. Longer minority carrier lifetime results in lower dark current, lower noise, higher operation temperature, and higher quantum efficiency. Applying this superlattice design to LWIR FPAs, it is expected to achieve higher quantum efficiency, lower dark current, higher specific directivity (D*) and reduced Noise Equivalent Temperature Difference (NEDT)

3. METHODS, ASSUMPTIONS, AND PROCEDURES

IDENTIFICATION AND SIGNIFICANCE OF THE PROBLEM OR OPPORTUNITY

Motivation

Over the past decades, the panel of applications for LWIR imagers has broadened considerably, including astronomy, medical applications, defense systems, etc. Most of the new technologies require fast (high frame-rate and short integration times), sensitive, uniform FPAs operating at high temperatures (>77K). As the imaging technology has matured it is also now becoming possible to consider imaging larger fields on view with a single camera, while simultaneously providing the resolution to see fine details. However, as a result, the arrays need to become larger and the pixels smaller as the number of pixels increases. This requires developing novel new solutions that provide higher performance while scaling to larger array sized without sacrificing manufacturability.

Commercially available infrared FPAs in the long-wave infrared include microelectromechanical systems (MEMS) arrays transducers, Quantum Well Photo-detectors (QWIP) and Mercury Cadmium Telluride (HgCdTe or MCT) compounds. However due to their intrinsically slow thermal time constant, which is on the order of 10 ms, MEMS are not fast enough for critical applications. QWIP demonstrate a faster response, however for wavelengths longer than 10 μm, the dark current levels of QWIP would significantly limit the FPA operating temperature.[1] The current state-of-the-art infrared detection technology in the LWIR is based on MCT materials, and can achieve excellent performances in term of sensitivity and speed at 9 and

---

1 M. Chu, S. Terterian, D. Walsh, H. K. Gurgenian, S. Mesropian, R. J. Rapp, and W. D. Holley, "Recent progress on LWIR and VLWIR HgCdTe focal plane arrays," Proc. of SPIE 5783, 243 (2005).

Approved for public release; distribution is unlimited.

12[2,3] μm. However, the spatial uniformity of II-VI HgCdTe compounds is very poor at the compositions needed for LWIR detectors. Very tight control of the cadmium mole fraction must be maintained in order to have a uniform cutoff wavelength and thus a uniform pixel response across the wafer. This limits the array yield which drives the cost of focal plane arrays prohibitively high and makes large-format arrays nearly impossible to realize in the LWIR.

InAs/GaSb Type-II Superlattices

InAs/GaSb Type-II superlattices, illustrated in Figure 1, are a developing new technology for the realization of LWIR imaging sensors. Invented by Nobel Laureate Leo Esaki, InAs/GaSb Type-II superlattices (T2SLs) have become an attractive material for infrared detection technology, due to the intrinsic advantages that they have over the MCT material system.[4] The strong bonding between group III and group V elements leads to very stable materials and high uniformity.[5] The band alignment of T2SLs creates an effective energy gap that can be flexibly tuned across the entire infrared regime via precise control of the interface composition and layer thicknesses, without introducing large strain. Owing to its coupled quantum well-based design, the cutoff wavelength across a typical 3" wafer is relatively insensitive to normal variations in layer thicknesses[6], and thus uniform infrared materials can be grown. Not only does this have ramifications for device performance but from a cost and yield standpoint the advantages are very clear.

2 A.S. Gilmore, J. Bangs, A. Gerrish, A. Stevens, B. Starr, "Advancements in HgCdTe VLWIR Materials," Proc. of SPIE 5783, 223 (2005).

3 A. Manissadjian, P. Tribolet, G. Destefanis, E. De Borniol, "Long wave HgCdTe staring arrays at Sofradir: From 9 μm to 13+ μm cut-offs for high performance applications," Proc. of SPIE 5783, 231 (2005).

4 Manijeh Razeghi, "Focal plane arrays in type II-superlattices," USA Patent No. 6864552 (2005).

5 H. Mohseni, A. Tahraoui, J. Wojkowski, M. Razeghi, G. J. Brown, W. C. Mitchel, Y. S. Park, "Very Long Wavelength Infrared Type-II Detectors Operating at 80K," Appl. Phys. Lett. 77, 1572 (2000).

6 Nguyen Binh-Minh, Chen Guanxi, Hoang Minh-Anh, and M. Razeghi, "Growth and Characterization of Long-Wavelength Infrared Type-II Superlattice Photodiodes an A 3-in Gasb," IEEE Journal of Quantum Electronics, 47 (5), 686-690 (2011).

Approved for public release; distribution is unlimited.

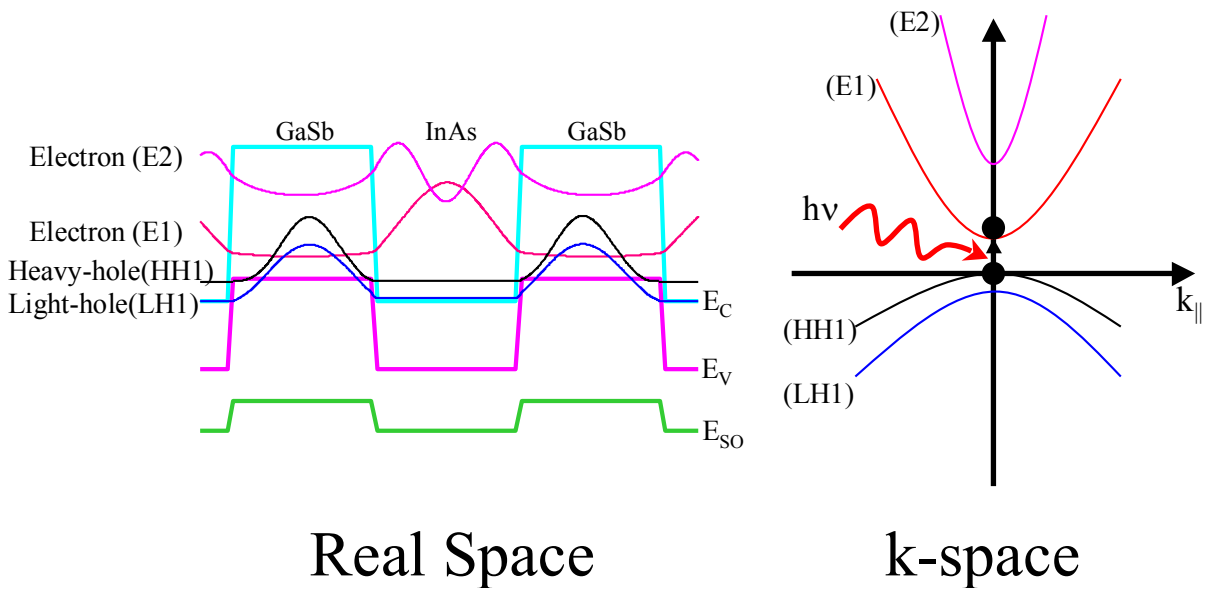

Figure 1. Illustration of the overlap of electron and hole wave function in InAs/GaSb superlattice and direct bandgap nature of the Type-II structure.

Auger recombination, which is a limiting factor for high temperature operation of infrared detectors, can be suppressed by manipulating the superlattice to control the band structure.[2] Compared to MCT and most of the small bandgap semiconductors that have very small electron and hole effective mass, the effective mass in T2SLs is relatively large, due to its special design which involves the interaction of electrons and holes via tunneling through adjacent barriers. The larger effective mass reduces the tunneling current, which is a major contributor to the dark current of MCT detectors. Moreover, the capability of band-structure engineering opens the horizon for exploring novel device architectures that are unthinkable using simple binary or ternary compound semiconductor band alignments like MCT. As an example, recent research has proposed a novel variant of T2SL, the M-structure superlattice,[7] with large effective mass and large tunability of band edge energies.[8] The structure has been shown to efficiently reduce the dark current in photovoltaic detectors.[9] Due to all these fundamental properties, T2SL has experienced a rapid development over the past decade (Figure 2-a) and its performance has reached a level comparable to state of the art MCT detectors (Figure 2-b).

7 B. M. Nguyen, M. Razeghi, V. Nathan, and Gail J. Brown, "Type-II M structure photodiodes: an alternative material design for mid-wave to long wavelength infrared regimes," Proceeding of SPIE, p. 64790S (2007).

8 Binh-Minh Nguyen, Darin Hoffman, Pierre-Yves Delaunay, Edward Kwei-Wei Huang, Manijeh Razeghi, and Joe Pellegrino, "Band edge tunability of M-structure for heterojunction design in Sb based type II superlattice photodiodes," Applied Physics Letters **93** (16), 163502 (2008).

9 Binh-Minh Nguyen, Darin Hoffman, Pierre-Yves Delaunay, and Manijeh Razeghi, "Dark current suppression in type II InAs⁄GaSb InAs⁄GaSb superlattice long wavelength infrared photodiodes with M-structure barrier," Applied Physics Letters **91** (16), 163511 (2007).

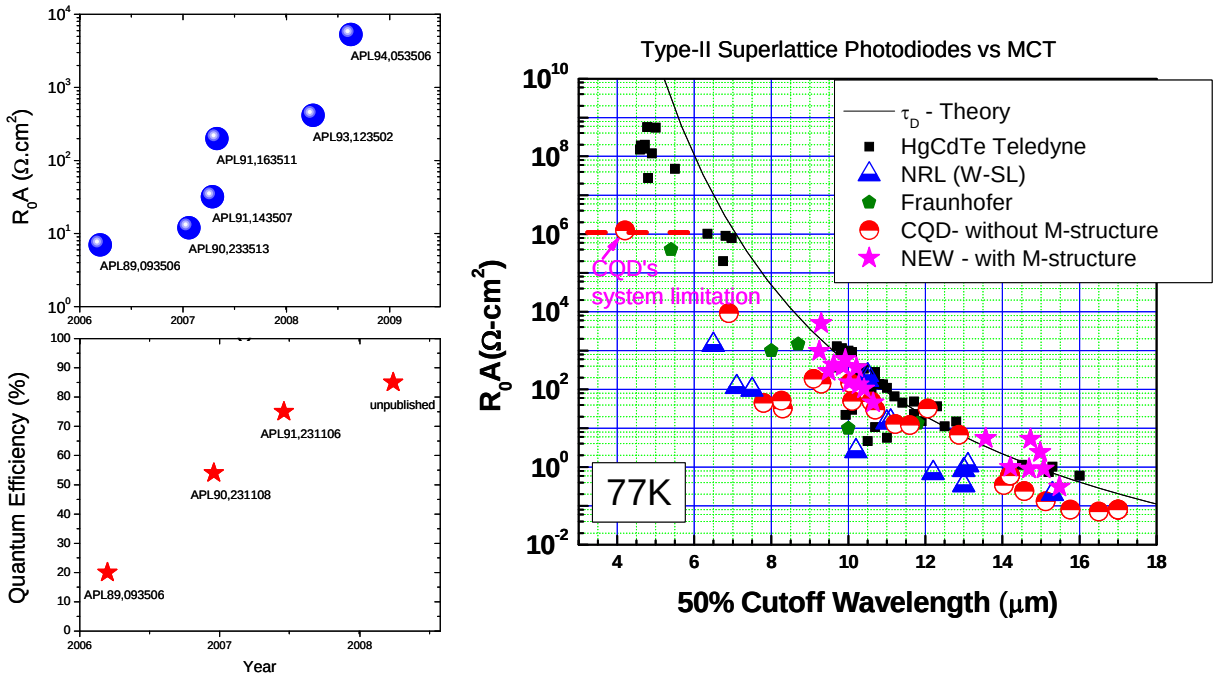

Figure 2. a) Steady progress of T2SL based photodetectors b) Performance comparison between T2SL and state of the art MCT detectors

InAs/InAs$_{1-x}$Sb$_x$ Type-II Superlattices

In addition to InAs/GaSb T2SLs, which have many potential advantages over bulk HgCdTe for infrared photodetector materials[10] and have been the most investigated T2SLs, recent efforts have been invested to develop new superlattice designs. The objective for most of these efforts is demonstration of T2SLs with longer minority carrier lifetime and higher mobility compare to InAs/GaSb T2SLs.[11,12] In a photodiode, as illustrated in Figure 3, photo-generated carriers from the region that is more than one diffusion length away from the depletion region will not contribute to the photo-current since they recombine before reaching the edge of the junction. The diffusion length L is related to minority carrier lifetime τ via the diffusivity D as follows:

$$L = \sqrt{D\tau} \qquad (1)$$

where the diffusivity is linked to the mobility μ by the Einstein relation:

$$D = \frac{\mu k_B T}{q} \qquad (2)$$

where k_B is the Boltzmann constant, T is the temperature and q is the electron charge. From these equations it is clear that a material with longer minority carrier lifetime and higher mobility will have a longer diffusion length, and thus better optical efficiency.

---

10 D. R. Rhiger, "Performance Comparison of Long-Wavelength Infrared Type II Superlattice Devices with HgCdTe," J. Electron. Mater. 40, 1815 (2011).

11 G. Belenky, G. Kipshidze, D. Donetsky, S. P. Svensson, W. L. Sarney, H. Hier, L. Shterengas, D. Wang, and Y. Lin, "Effects of carrier concentration and phonon energy on carrier lifetime in type-2 SLS and properties of InAsSb alloys," Proc. SPIE 8012, 0120W (2011).

12 B. C. Connelly, G. D. Metcalfe, H. Shen, and M. Wraback, "Direct minority carrier lifetime measurements and recombination mechanisms in long-wave infrared type II superlattices using time-resolved photoluminescence," Appl. Phys. Lett. 97, 251117 (2010).

Approved for public release; distribution is unlimited.

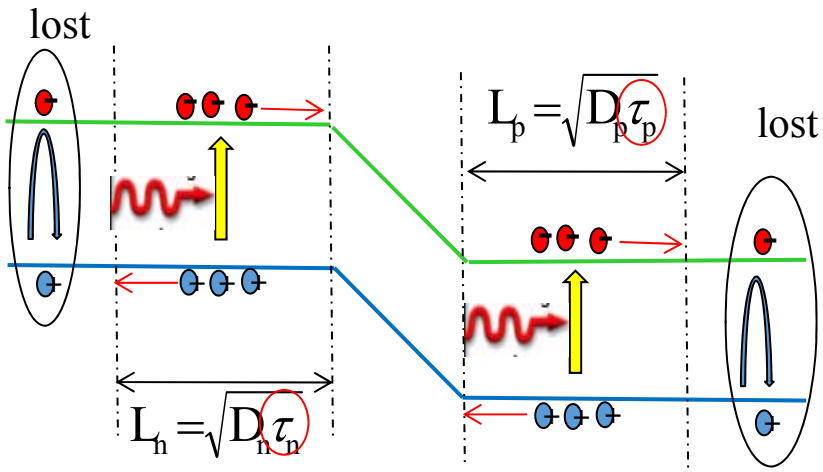

Figure 3. The carriers generated within a diffusion length of the junction are collected while the rest are lost

The dark current in a photodiode also depends on minority carrier lifetime. The dark current consists of four major components:

- diffusion
- generation-recombination
- band-to-band tunneling
- trap-assisted tunneling

The diffusion and generation-recombination components of the dark current strongly depend on minority carrier lifetime. By increasing the minority carrier lifetime, one can decrease the dark current density and increase quantum efficiency of the photodiode.

The limitation in minority carrier lifetime of InAs/GaSb T2SLs has been partially attributed to acceptor-like defects in GaSb rather than the interfaces.[13] With Gallium being the suspected culprit of the short minority carrier lifetime, InAs /$InAs_{1-x}Sb_x$ T2SL has the potential for longer lifetimes. The "stabilized Fermi level" due to intrinsic point defects in bulk InAs is expected to be above the conduction band edge,[14] rendering any midgap defect states inactive for Shockley–Read–Hall (SRH) processes. In comparison, the stabilized Fermi level for bulk GaSb is expected to be in the bandgap near the valence band edge, leaving the midgap states available for SRH recombination. Relatively high photoluminescence (PL) efficiencies for 4-11 µm emission from InAs/$InAs_{1-x}Sb_x$ T2SLs grown on GaAs with highly dislocated 1 µm $InAs_{1-x}Sb_x$ buffer layers also suggest that As-rich $InAs_{1-x}Sb_x$ alloys have comparatively low SRH recombination coefficients.[15] A minority carrier lifetime of 250 ns reported for bulk $InAs_{0.80}Sb_{0.20}$ having a PL peak at 5.4 µm at 77 K further supports the possibility that the InAs/$InAs_{1-x}Sb_x$ T2SLs may have longer lifetimes than those of the InAs/GaSb T2SLs. Theoretically calculated absorption of an 11µm InAs/$InAs_{1-x}Sb_x$ T2SL was

---

13 S. P. Svensson, D. Donetsky, D. Wang, P. Maloney, and G. Belenky, "Carrier lifetime measurements in InAs/GaSb strained layer superlattice structures," Proc. SPIE 7660, 76601V (2010).

14 W. Walukiewicz, "Defect Reactions at Metal-Semiconductor and Semiconductor-Semiconductor Interfaces," Proc. Mat. Res. Soc. Symp. 148, 137 (1989).

15 P. J. P. Tang, M. J. Pullin, S. J. Chung, C. C. Phillips, R. A. Stradling, A. G. Norman, Y. B. Li, and L. Hart, "4-11 mu m infrared emission and 300 K light emitting diodes from arsenic-rich InAs1-xSbx strained layer superlattices," Semicond. Sci. Technol. 10, 1177 (1995).

lower, but within a factor of two, than that of a 10 μm InAs/GaSb T2SL.[16] The theoretical study did not include SRH recombination, leaving open the possibility that in practice, the former T2SL may have higher absorption and a longer minority carrier lifetime than the latter due to interface and growth-related variations. The recent published results based on InAs/$InAs_{1-x}Sb_x$ T2SLs have not shown superior performance compare to the InAs/GaSb T2SLs both in midwave infrared (MWIR) and LWIR ranges.[17,18] However, private unpublished sources have confirmed that InAs/$InAs_{1-x}Sb_x$ T2SL-based photodetectors have demonstrated equal or better performance compare to InAs/GaSb T2SL-based photodetectors in MWIR regime. In addition, relatively simple interface structure and epitaxial growth is the other driving force for performing more investigation on InAs/$InAs_{1-x}Sb_x$ T2SL-based photodetectors.

4. LWIR NBN PHOTODETECTORS BASED ON INAS/$INAS_{1-X}SB_X$/$ALAS_{1-X}SB_X$ TYPE-II SUPERLATTICES

LWIR detection is important because the ambient temperature of a scene, for ground-based applications, is around 300 K, where the emission peak is ~9.8 μm–in the center of the LWIR atmospheric transmission window; this leads to a demand for sensitive LWIR photodetectors. The challenge for making LWIR photodetectors in this material system is reduction of its dark current density while maintaining good optical quantum efficiency in order to achieve background limited (photon-noise) infrared photodetection (BLIP).

In this work, we present LWIR nBn photodetectors based on InAs/$InAs_{1-x}Sb_x$ T2SLs with new barrier design that has shown a significant dark current reduction compare to prior results while maintaining low bias-dependent optical response. Thanks to the new barrier design, this nBn photodetector is BLIP at 77 K operating temperature and it stays BLIP up to 110 K.

The proposed nBn device architecture consists of two *n*-doped LWIR superlattices and a thin electron barrier which has zero valence band discontinuity with respect to the *n*-type LWIR regions. One of the *n*-type regions acts as the LWIR absorption region and the other one is used as a contact. Figure 4 (a) shows a schematic of the device design and the alignment of the conduction and valence bands. The LWIR superlattice design consists of 30/10 mono-layers (MLs) of InAs/$InAs_{0.50}Sb_{0.50}$, respectively, per period with a ~10 μm nominal cut-off wavelength at 77K while the electron barrier design consists of 4/3/4/3/4/9 MLs of InAs/$AlAs_{0.50}Sb_{0.50}$/InAs/$AlAs_{0.50}Sb_{0.50}$/InAs/$InAs_{0.50}Sb_{0.50}$, respectively, per period with a nominal cut-off wavelength of ~4 μm. Using $AlAs_{0.50}Sb_{0.50}$ instead of AlAs in the barrier design provides more flexibility. Because $AlAs_{0.50}Sb_{0.50}$ has a lower lattice mismatch to the GaSb substrate, it introduces less local strain to the crystalline structure of the superlattice and can be grown thicker compare to AlAs. Furthermore, inserting two spatially-separated $AlAs_{0.50}Sb_{0.50}$ high-bandgap layers inside the InAs quantum well (see Figure 4-b) helps us to achieve larger effective conduction band offset (~200 meV) compare to previous work (~150 meV) while maintaining high crystalline quality. We call this structure a saw-tooth superlattice.

---

[16] C. H. Grein, M. E. Flatte and H. Ehrenreich, "Comparison of Ideal InAs/InAsSb and InAs/InGaSb Superlattice IR Detectors," Proc on the 3rd International Symposium on Long Wavelength Infrared Detectors and Arrays: Physics and Applications III, Chicago, IL, 8–13 October 1995.

[17] E. H. Steenbergen, K. Nunna, L. Ouyang, B. Ullrich, D. L. Huffaker, D. J. Smith, and Y.-H. Zhang, "Strain-balanced InAs/InAsSb type-II superlattices grown by molecular beam epitaxy on GaSb substrates," Journal of Vacuum Science & Technology B: Microelectronics and Nanometer Structures **30,** 02B107 (2012).

[18] T. Schuler-Sandy, S. Myers, B. Klein, N. Gautam, P. Ahirwar, Z.-B. Tian, T. Rotter, G. Balakrishnan, E. Plis, and S. Krishna, "Gallium free type II InAs/InAsxSb1-x superlattice photodetectors," Applied Physics Letters **101,** 071111 (2012).

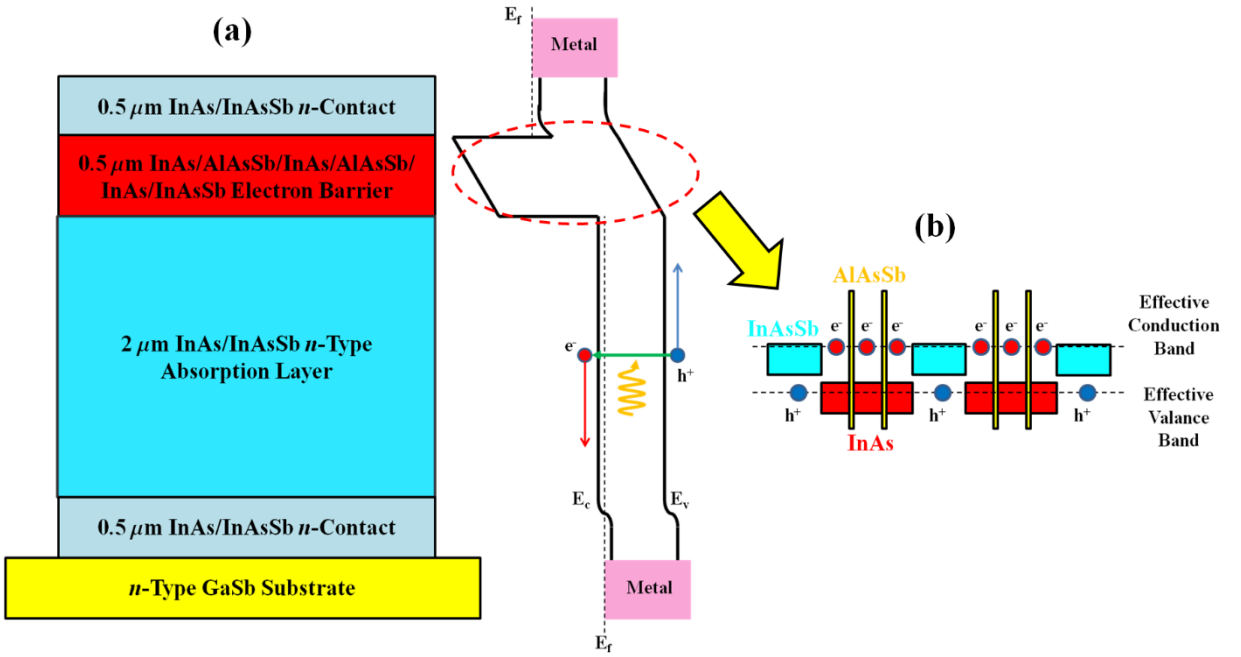

Figure 4. (a) The schematic diagram and working principle of the nBn photodetector. b) The band alignment and the creation of an effective bandgap in InAs/AlAs$_{1-x}$Sb$_x$/InAs/AlAs$_{1-x}$Sb$_x$/InAs/InAs$_{1-x}$Sb$_x$ saw-tooth superlattice of the barrier.

In Figure 4a the barrier blocks the transport of majority electrons, while allowing the diffusion of minority holes and photo-generated carriers from the absorption region. And in Figure 4b the colored rectangles represent the forbidden bandgap of the semiconductor materials. The atomic engineering capability of T2SLs enable perfect alignment in the valence bands of the absorption region and the barrier.

The device was grown on a Te-doped *n*-type (10^{17}cm^{-3}) GaSb wafer using a solid source molecular beam epitaxy (SSMBE) reactor equipped with group III SUMO® cells and group–V valved crackers. The growth started with a 100 nm GaSb buffer layer to smooth out the surface, then, a 0.5 μm *n*-doped InAs$_{0.91}$Sb$_{0.09}$ buffer layer (10^{18} cm^{-3}) was grown, which was followed by a 0.5 μm *n*-contact (10^{18} cm^{-3}), a 2 μm-thick *n*-type absorption region (10^{16}cm^{-3}), a 0.5 μm electron barrier, and a 0.5 μm *n*-contact. The *n*-contacts and absorption region share the same superlattice design and silicon (Si) was used as the *n*-type dopant in this device.

After the epitaxial growth, the material quality was assessed using high resolution X-ray diffraction (HR-XRD) and atomic force microscopy (AFM). The satellite peaks in the HR-XRD scan show that the overall periods of the absorption region and barrier superlattices were about 118 and 79 Å, respectively. The lattice mismatch between the GaSb substrate and the device structure was less than 1000 ppm, as we expected. The AFM showed a good surface morphology with clear atomic steps and a root mean squared (RMS) roughness of 1.2 Å over a 10×10 μm^2 area.

After material quality assessment, the grown material was processed into a set of unpassivated mesa-isolated test structures with device sizes ranging from 100×100 to 400×400 μm^2 using standard photo-lithographic processing technique followed by mesa definition using BCl_3:Ar^+ dry etching and citric acid treatment to remove dry etch residues. Top and bottom metal contacts were formed using electron beam deposited Ti/Pt/Au. The photodetectors were left unpassivated but special attention was paid during the processing steps by performing many surface cleaning steps

Approved for public release; distribution is unlimited.

using different solvents in order to minimize the surface leakage. Then, the sample was wire-bonded to a 68 pin leadless ceramic chip carrier (LCCC) and loaded into a cryostat for both optical and electrical characterization at temperatures ranging from 77 to 130 K.

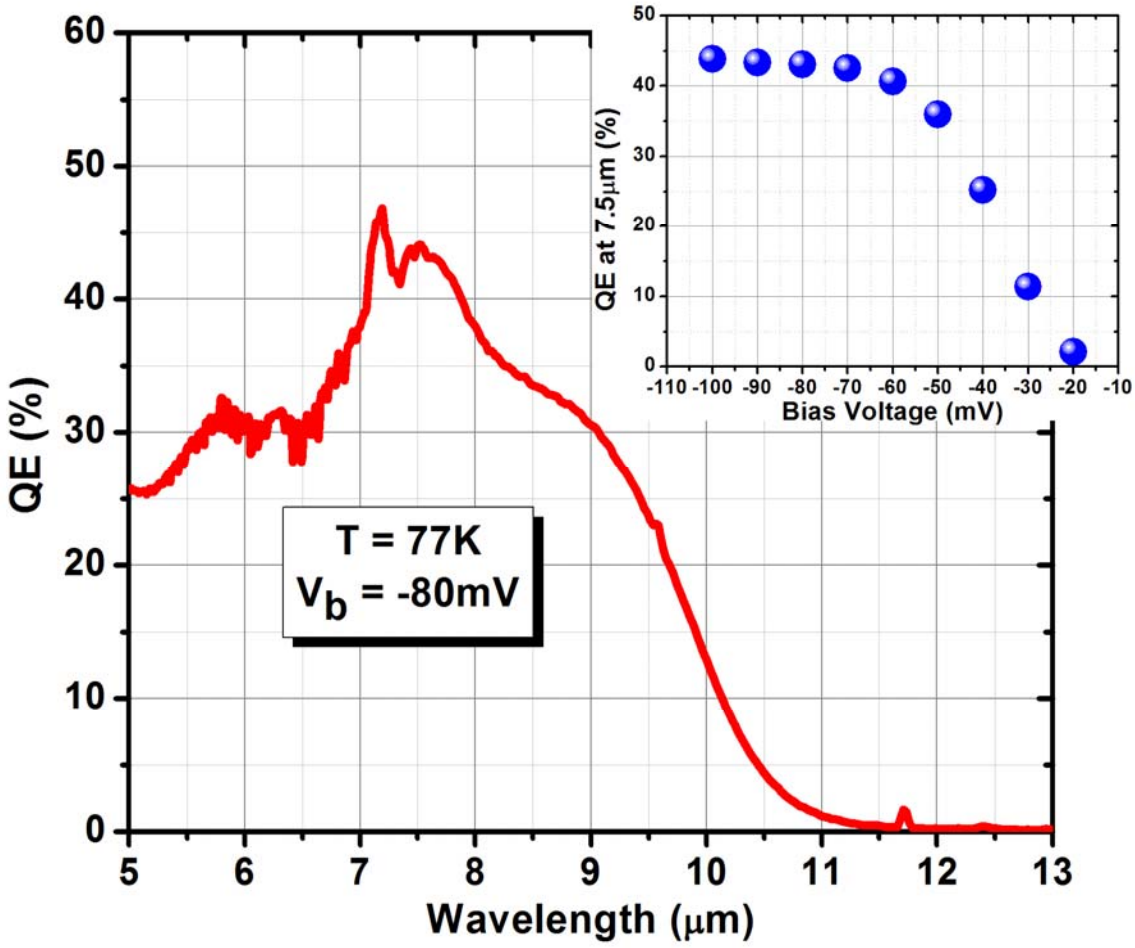

Figure 5. Saturated quantum efficiency spectrum of the device at -80mV applied bias voltage in front-side illumination configuration without any anti-reflection coating.

The optical characterization was done at temperatures between 77 and 130 K under front-side illumination without any anti-reflection (AR) coating having been applied to the photodetector. A Bruker IFS 66 v/S Fourier transform infrared spectrometer (FTIR) was used to measure the spectral response of the photodetectors. The responsivity and quantum efficiency of the photodetector were measured using a calibrated blackbody source at 1000 °C. Figure 5 shows the optical performance; the device exhibits a 50% cut-off wavelength of ~10 μm at 77 K (see Figure 5 inset) which corresponds with the designed band structure. Figure 5, inset quantum efficenency of the device 7. *5 μm* in front-side illumination configuration as a function of applied bias voltage *(V_b)*. The device responsivity reaches a peak of 2.65 A/W, corresponding to quantum efficiency (QE) of 43% for a device with 2 μm-thick absorption region. An applied bias voltage is required in this device to extract full optical signal which is a characteristic of an nBn unipolar device. This bias voltage is usually high (V_b > 500mV) for nBn devices because of the large valence band discontinuity between the absorption layer and the electron barrier; but, this device requires much lower bias voltage to fully extract the optical signal because of the new saw-tooth superlattice-

based barrier leads to nearly–perfect valence band continuity. The QE starts to increase linearly with increasing reverse bias voltage from 20 mV and saturates at 80 mV, as shown in the inset of the Figure 5. This is a very good saturation value for an nBn device, and will allow the devices to be operated at small dark currents.

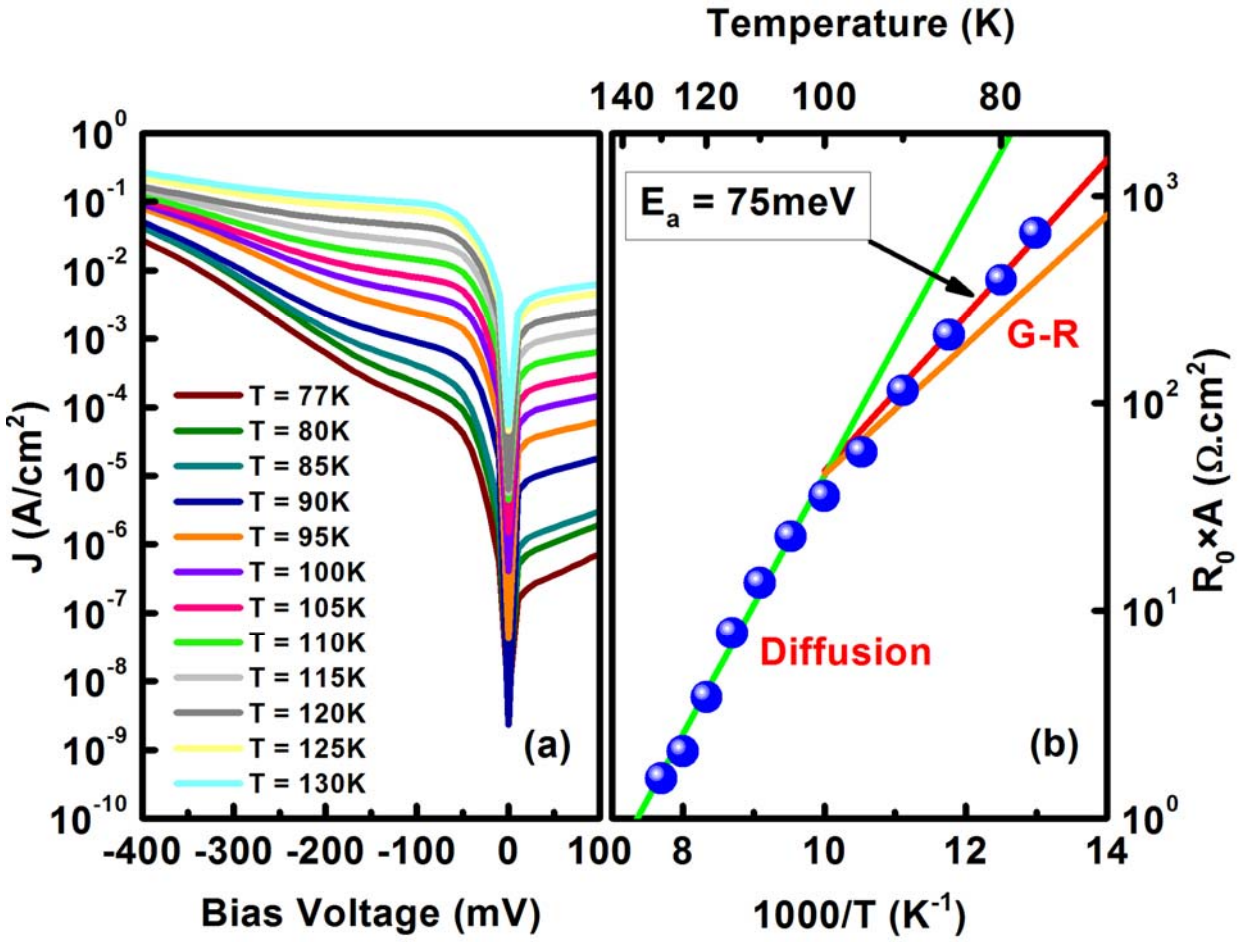

Figure 6. (a) Dark current density vs. applied bias voltage (b) R×A vs. 1/T; the sample exhibited an Arrhenius type behavior with associated activation energy (E_a) of about ~75 meV below 100 K.

Figure 6 shows the electrical performance of the nBn device measured when covered by a cold-shield. Figure 6(a) presents the dark current density versus applied bias voltage characteristics of the device at different temperatures ranging from 77 to 130 K. At 77 K, the sample exhibits a dark current density of 8×10^{-5} A/cm^2 under -80 mV applied bias and a differential-resistance area product (R×A) of 664 Ω·cm^2 under the same bias voltage. The variation of R×A versus inverse temperature (1/T) from 77 to 130 K is shown in Figure 6(b). Below 100 K, the R×A exhibits an Arrhenius-type behavior with extracted associated activation energy of about ~75 meV which is smaller than the bandgap energy of the photodetector (~124 meV). At temperatures above 100K, the device dark current is completely diffusion-limited. This indicates that the dark current of the device is not completely dominated by the diffusion mechanism below 100 K. However, above 100 K the device electrical performance becomes totally diffusion-limited. This behavior suggests that there is still room for further improvement in the electrical performance of the photodetectors

Approved for public release; distribution is unlimited.

at temperatures below 100 K by suppressing dark current mechanisms such as generation-recombination (G-R).

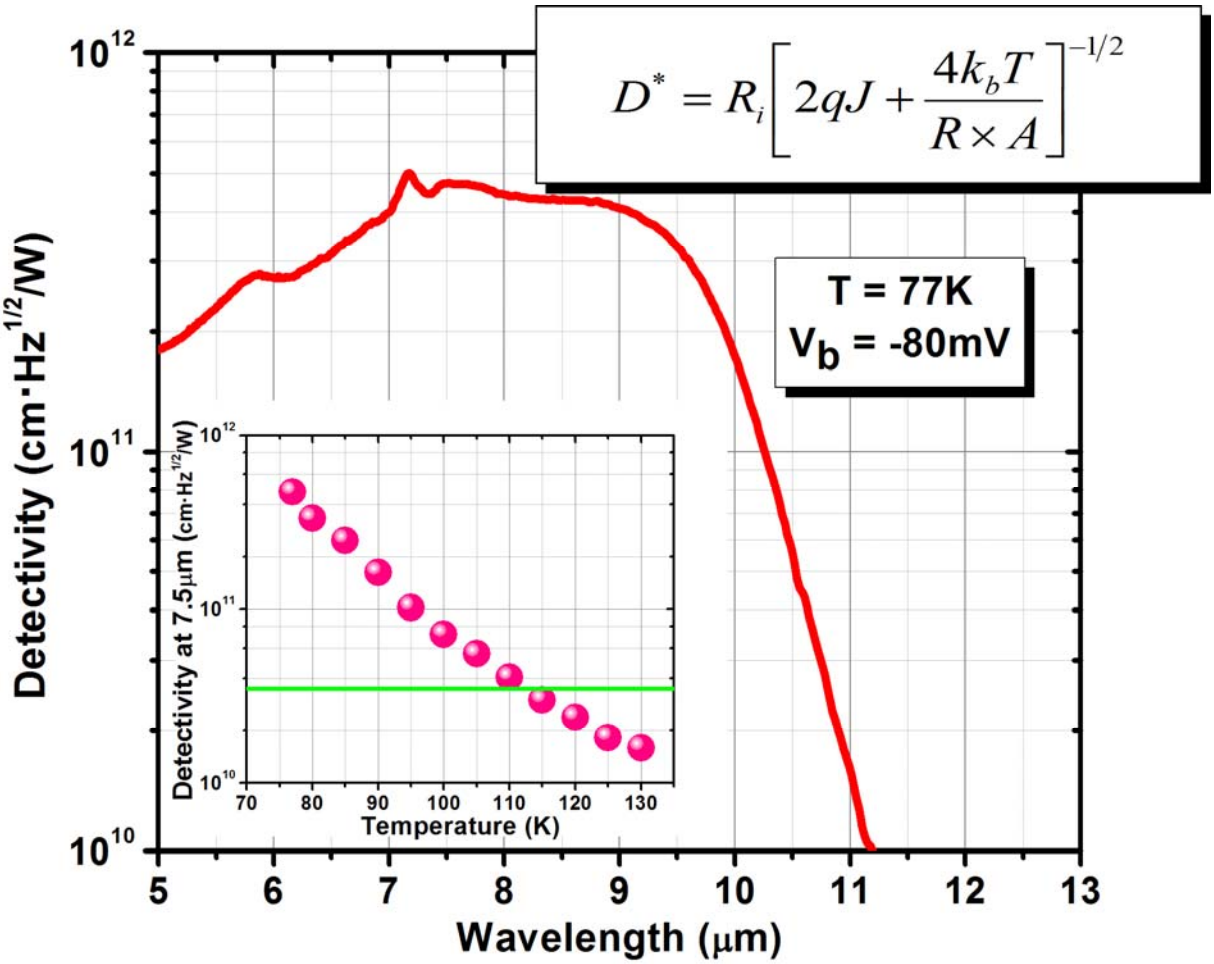

Figure 7. Saturated specific detectivity spectrum of the device at -80mV applied bias voltage in front-side illumination configuration without any anti-reflection coating.

Inset: Specific detectivity of the device versus operating temperature at 7.5 μm under front-side illumination. The green line is the BLIP detectivity for an ideal photodetector with 2π field of view (FOV) with 300 K background. The specific detectivity is calculated based on the equation in the inset, where R_i is the device responsivity, J is the dark current density, R×A is the differential resistance×area product, k_b is the Boltzmann constant, and T is the operating temperature. After the electrical and optical characterization, the specific detectivity was calculated by taking into account both the Johnson thermal noise and the electrical shot noise at the operational bias. The devices exhibit saturated dark current shot noise limited specific detectivity (D^*) of 4.72×10^{11} cm·$\sqrt{Hz}$/W (at a peak responsivity of 7.5 μm) under -80 mV of applied bias (Figure 7). In order to determine the BLIP temperature, we used the point when the specific detectivity of the photodetector is less than the value for an ideal photodetector with 100% QE and a fully immersed 300 K background with a 2π field of view (FOV). Figure 7 (inset) presents the specific detectivity of the photodetector at 7.5 μm versus operating temperature. As the temperature increases, the specific detectivity reduces and intersects the

BLIP specific detectivity (green line) slightly beyond 110 K. In Figure 7 the inset: Specific detectivity of the device versus operating temperature at 7.5 μm under front-side illumination. The green line is the BLIP detectivity for an ideal photodetector with 2π FOV with 300 K background. The specific detectivity is calculated based on the equation in the inset, where R_i is the device responsivity, J is the dark current density, R×A is the differential resistance×area product, k_b is the Boltzmann constant, and T is the operating temperature.

5. RESULTS AND DISCUSSION

TEST SAMPLES DELIVERED TO AFRL (FEBRUARY 2017)

LWIR sample with a 50% cut-off wavelength of 9.5 μm at 77K.

- This is a **MWIR sample** with a **50% cut-off wavelength of 5.05 μm at 150K**.
- The sample has a **QE = 54%** and **R_i = 2.04 A/W** at 4.66μm and V_b = 0V at 150K.
- The dark current density is **2.3×10^{-5} A/cm^2** at V_b = -50mV and 150K.
- The specific detectivity is **7.26×10^{11} Jones** at V_b = -50mV and 150K.

MWIR sample with a 50% cut-off wavelength of 5.05 μm at 150K.

- This is a LWIR sample with a 50% cut-off wavelength of 9.5 μm at 77K.
- The sample has a QE = 32% and R_i = 2.1 A/W at 8.2μm and V_b = -220mV at 77K.
- The dark current density is 1.4×10^{-4} A/cm^2 at V_b = -220mV and 77K.
- The specific detectivity is 2.87×10^{11} Jones at V_b = -220mV and 77K.

6. CONCLUSION

In conclusion, we have reported the design, growth, and characterization of high-performance LWIR nBn photodetectors based on InAs/$InAs_{1-x}Sb_x$ T2SLs on GaSb substrates. A new saw-tooth superlattice design was used to implement the electron barrier of the device. The devices exhibited a 50% cut-off wavelength of 10 μm at 77 K. At the peak responsivity, the photodetector exhibited QE and responsivity of 43% and 2.65 A/W, respectively, under front-side illumination and without any AR coating. At -80 mV, the device exhibited dark current density and R×A of 8×10^{-5} A/cm^2 and 664 Ω·cm^2, respectively, at 77 K. At 7.5 μm, the device exhibited a saturated dark current shot noise limited specific detectivity of 4.72×10^{11} cm·$\sqrt{Hz}$/W at 77 K. Finally, the device showed BLIP performance up to an operating temperature of 110 K; this requires less stringent cooling requirements, which makes T2SL a viable option for third generation FPAs.

ACRONYMS

1/T	inverse temperature
AFM	Atomic force microscopy
AR	anti-reflection
BLIP	background limited infrared photodetection
D*	directivity
FOV	field of view
FPA	focal plane arrays
FTIR	fourier transform infrared spectrometeter
G-R	generation-recombination
HgCdTe or MCT	mercury cadmium telluride
HR-XRD	high resolution x-ray
J	dark current density
k_b	Boltzmann constant
LCCC	leadless ceramic chip carrier
LWIR	long-wavelength infrared
MEMS	microelectromechanical systems
ML	mono-layers
MWIR	midwave infrared
NEDT	Noise equivalent temperature difference
PL	photoluminescence
QE	quantum efficiency
QWIP	quantum well phot-detectors
Ri	device responsivity
RMS	root mean squared
RxA	differential-resistance area product
SRH	Shockly-Read-Hall
SSMBE	solid source molecular bean epitaxy
Si	silicon
T	Temperature
T2SL	Type-II superlattices

DISTRIBUTION LIST

DTIC/OCP 8725 John J. Kingman Rd, Suite 0944 Ft Belvoir, VA 22060-6218	1 cy
AFRL/RVIL Kirtland AFB, NM 87117-5776	2 cys
Official Record Copy AFRL/RVSW/David Cardimona	1 cy

Approved for public release; distribution is unlimited.

(This page intentionally left blank)